ACSNANO

www.acsnano.org

ARTICLE

Heterometal-Doped M_{23} (M = Au/Ag/Cd) Nanoclusters with Large Dipole Moments

Yingwei Li,[¶] Michael J. Cowan,[¶] Meng Zhou, Michael G. Taylor, He Wang, Yongbo Song,* Giannis Mpourmpakis,* and Rongchao Jin*

Cite This: *ACS Nano* 2020, 14, 6599–6606

Read Online

ACCESS | Metrics & More | Article Recommendations | Supporting Information

ABSTRACT: Dipole moment (μ) is a critical parameter for molecules and nanomaterials as it affects many properties. In metal–thiolate (SR) nanoclusters (NCs), μ is commonly low (0–5 D) compared to quantum dots. Herein, we report a doping strategy to give giant dipoles (~18 D) in M_{23} (M = Au/Ag/Cd) NCs, falling in the experimental trend for II–VI quantum dots. In M_{23} NCs, high μ is caused by the Cd–Br bond and the arrangement of heteroatoms along the C_3 axis. Strong dipole–dipole interactions are observed in crystalline state, with energy exceeding 5 kJ/mol, directing a "head-to-tail" alignment of $Au_{22-n}Ag_nCd_1(SR)_{15}X$ (SR = adamantanethiolate) dipoles. The alignment can be controlled by μ *via* doping. The optical absorption peaks of M_{23} show solvent polarity-dependent shifts (~25 meV) with negative solvatochromism. Detailed electronic structures of M_{23} are revealed by density functional theory and time-dependent DFT calculations. Overall, the doping strategy for obtaining large dipole moments demonstrates an atomic-level design of clusters with useful properties.

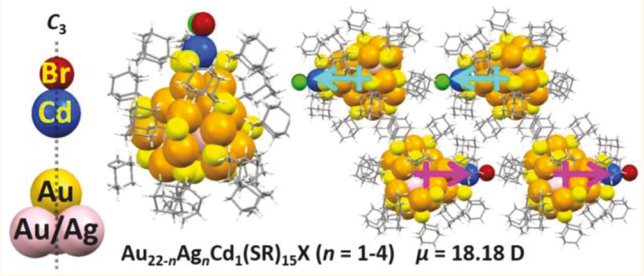

KEYWORDS: *alloy nanoclusters, atomic precision, dipole moment, dipole–dipole interaction, controlled assembly*

To control the self-assembly of nanocrystals to obtain superstructures with outstanding thermoelectric,[1] photovoltaic, optical, electrical,[2] magnetic,[3,4] chiroptical,[5] and other properties[6] for applications, the uniformity of the building blocks is critical for precise control over the collective properties of the superstructures.[7−9] High dipole moment (μ) of nanocrystals is commonly observed in semiconductor nanocrystals, that is, quantum dots (QDs). The presence of a permanent μ is crucial in interpreting the self-assembly behavior of nanocrystals in solution.

Guyot-Sionnest et al. used dielectric dispersion measurements to demonstrate the large μ of CdSe and ZnSe nanocrystal colloids, indicating large μ might be an intrinsic attribute to all nonmetal nanoparticles with surface localized charges.[10,11] However, metal nanocrystals (*e.g.*, Ag nanocrystals of 55 Å diameter) did not exhibit a permanent dipole moment,[11] or it was too low to be detected. The strong dipole–dipole interaction was reported to drive the self-organization of CdTe nanocrystals into "pearl-necklace" aggregates and subsequent recrystallization into nanowires with the same diameter as that of nanocrystals.[12] The dipolar driving force also directs the formation of PbSe nanowires through one-dimensional oriented attachment.[13] Electronic energy transfer was reported to occur between CdSe QDs arising from dipole–dipole interdot interactions.[14] Energy transfer from semiconductor nanocrystals to the plasmonic components in the self-assembled binary superlattices of CdSe and Au nanocrystals was also reported.[15]

Recently, ligand-protected metal nanoclusters (NCs) of atomic precision in the range of 1–3 nm diameter have emerged as promising nanomaterials.[16] Such NCs provide great opportunity to correlate the atomic-level structures of NCs with their properties. However, there are still fundamental properties that we do not yet understand in nanoclusters, especially the intercluster interactions,[17,18] mainly due to the existence of surface ligands that offer stability to the NCs and prevent the couplings between individual NCs. van der Waals forces (less than $0.5k_BT$ in energy for $T \approx 298$ K) are usually not sufficient to achieve irreversibly aggregated superstructures under ambient conditions. On the basis of the total structures solved by X-ray crystallography, the dipole moments of a series of ten Au-thiolate (SR) NCs (the number of Au atoms ranging

Received: February 4, 2020
Accepted: April 14, 2020
Published: April 14, 2020

https://dx.doi.org/10.1021/acsnano.0c01000
ACS Nano 2020, 14, 6599–6606

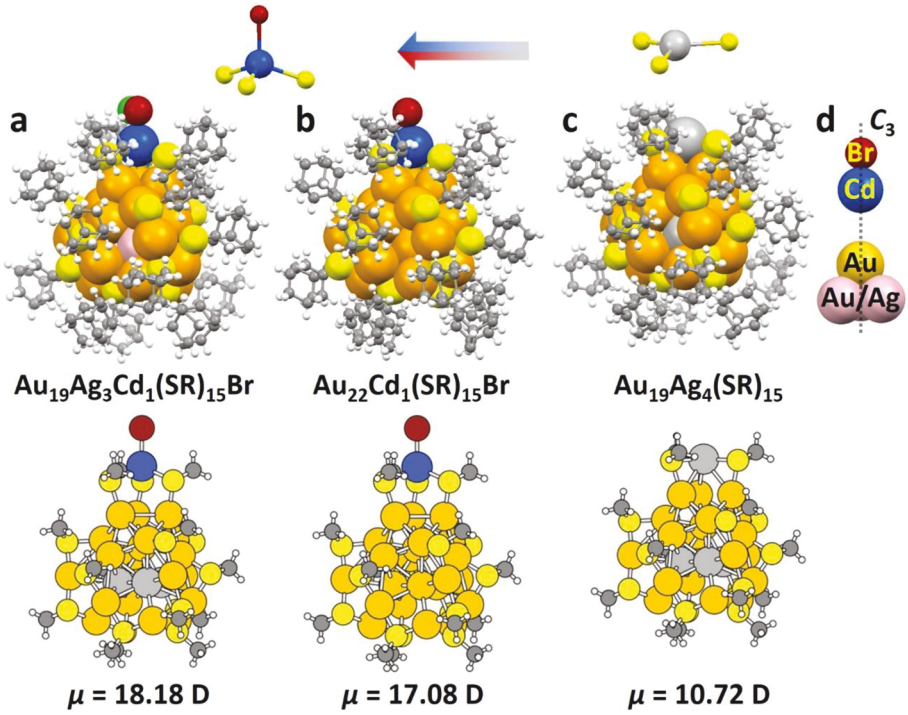

Figure 1. Crystal structures and corresponding structures fully optimized with DFT for (a) $Au_{22-n}Ag_nCd_1(SR)_{15}X$ (n = 1−4) optimized as $Au_{19}Ag_3Cd_1(SR)_{15}Br$, (b) $Au_{22}Cd_1(SR)_{15}Br$, and (c) $Au_{19}Ag_4(SR)_{15}$ (SR = SAdm in experiment, SR = SCH_3 in calculation). (d) Atom arrangement with a sequence of Br−Cd-central Au-M_3 triangle (M= Au/Ag) along the quasi-C_3 axis in $Au_{22-n}Ag_nCd_1(SR)_{15}X$. Color labels: yellow = Au, light gray = Ag, pink = Au/Ag, blue = Cd, maroon = Br, green = Cl, light yellow = S, gray = C, and white = H.

from 21 to 133) have recently been calculated to be 0−5 D,[19] much smaller than those of quantum dots.[10,11] Thus, no strong dipole−dipole interactions among the NCs in the solid state or interactions between NCs and solvent molecules can be expected.

In this work, we report trimetallic $Au_{22-n}Ag_nCd_1(SAdm)_{15}X$ (X = Br/Cl) and bimetallic $Au_{22}Cd_1(SAdm)_{15}Br$ NCs in which a $Cd_1(SAdm)_3X$ motif with Cd-X ionic bond is introduced onto the surface of the NCs (SAdm = adamantanethiolate). High μ of ∼18 D is found for $Au_{19}Ag_3Cd_1(SAdm)_{15}Br$ and ∼17 D for $Au_{20}Cd_1(SAdm)_{15}Br$, which fits into the size versus dipole moment plot of CdSe and ZnSe QDs. Furthermore, the large dipole−dipole interactions between $Au_{22-n}Ag_nCd_1(SAdm)_{15}Br$ NCs (>5 kJ/mol) control their assembly in the crystal states, resulting in a "head-to-tail" 1D oriented alignment of these NC dipoles. The interactions between NCs and solvent molecules are also reflected in the solvent polarity-dependent peak shifts (by ∼25 meV), indicating charge-transfer absorption with negative solvatochromism. Density functional theory (DFT) and time-dependent DFT (TDDFT) calculations were performed on the M_{23} series, revealing the highly polar groun state and a separation between major atomic contributors of the occupied and unoccupied frontier Kohn−Sham (KS) orbitals. The excited states of the M_{23} series are also highly polar.

RESULTS AND DISCUSSION

The syntheses of $Au_{22-n}Ag_nCd_1(SAdm)_{15}X$ NCs followed a method of coreduction of Au^I−SAdm, Ag^I−SAdm, and Cd^{II}−SAdm by $NaBH_4$ (see Supporting Information for details). In the absence of Ag^I−SR, controlling the molar ratio of Au:Cd= 12:1 gave rise to $Au_{22}Cd_1(SAdm)_{15}Br$, whereas coreduction of trimetallic precursors of Au:Ag:Cd = 10:0.3:1 and 10:0.5:1 (molar ratios) produced $Au_{22-n}Ag_nCd_1(SAdm)_{15}X$ with n = 1−4 and 2−8, respectively, where X = Br/Cl. All crystallizations were performed by layer diffusion of ethanol into the dichloromethane solutions of the NCs. The UV−vis and ESI-MS spectra of the NCs are given in Figures S1−S4.

The structures of $Au_{22-n}Ag_nCd_1(SAdm)_{15}X$ (avg. n = 1.87, X = $Br_{0.84}Cl_{0.16}$ by X-ray crystallography, Table S1) and $Au_{22}Cd_1(SAdm)_{15}Br$ (Table S2) are shown in Figure 1a and b. The NCs possess an icosahedral M_{13} kernel (M = Au/Ag) in which Ag atoms are found in the bottom M_3 triangle (Figure 1a). The kernel is protected by a $Cd_1(SAdm)_3Br$ motif at the top and three $Au_3(SAdm)_4$ staple motifs at the bottom. We note that although ESI-MS reveals n = 1−4 for $Au_{22-n}Ag_nCd_1(SAdm)_{15}X$ (Figure S2), the average number of Ag in the resolved crystal is n = 1.87, and the ∼2 Ag atoms are almost equally distributed at the M_3 positions due to the C_3 symmetry of the NC. When increasing the Ag ratio in the precursor, trimetallic NCs with n = 2−8 (n = 3 being the highest peak) are obtained (Figure S3), indicating the number of Ag can be controlled experimentally. Because of the largest peak height at n = 3 in the ESI-MS (Figure S3), n = 3 is the most favorable number of Ag in solution. Thus, our DFT calculations are based on $Au_{19}Ag_3Cd_1(SAdm)_{15}Br$ NC (*vide infra*). Compared to the previously reported $Au_{19}Ag_4(SAdm)_{15}$ (protected by the same ligand, shown in Figure 1c as ref 20), the difference lies in the replacement of the $Ag_1(SAdm)_3$ motif in $Au_{19}Ag_4(SAdm)_{15}$ by a $Cd_1(SAdm)_3Br$ motif herein, which is critical to achieve the giant dipole moment (*vide infra*).

It is well-known that ligands may have an impact on the dipole moment of nanoparticles. As to atomically precise NCs, previous work revealed that a series of ten Au-SR NCs (ranging from $Au_{21}(SR)_{15}$ to $Au_{133}(SR)_{52}$)[21,22] have μ no larger than 5 D.[19] Importantly, the work concludes that the

https://dx.doi.org/10.1021/acsnano.0c01000
ACS Nano 2020, 14, 6599−6606

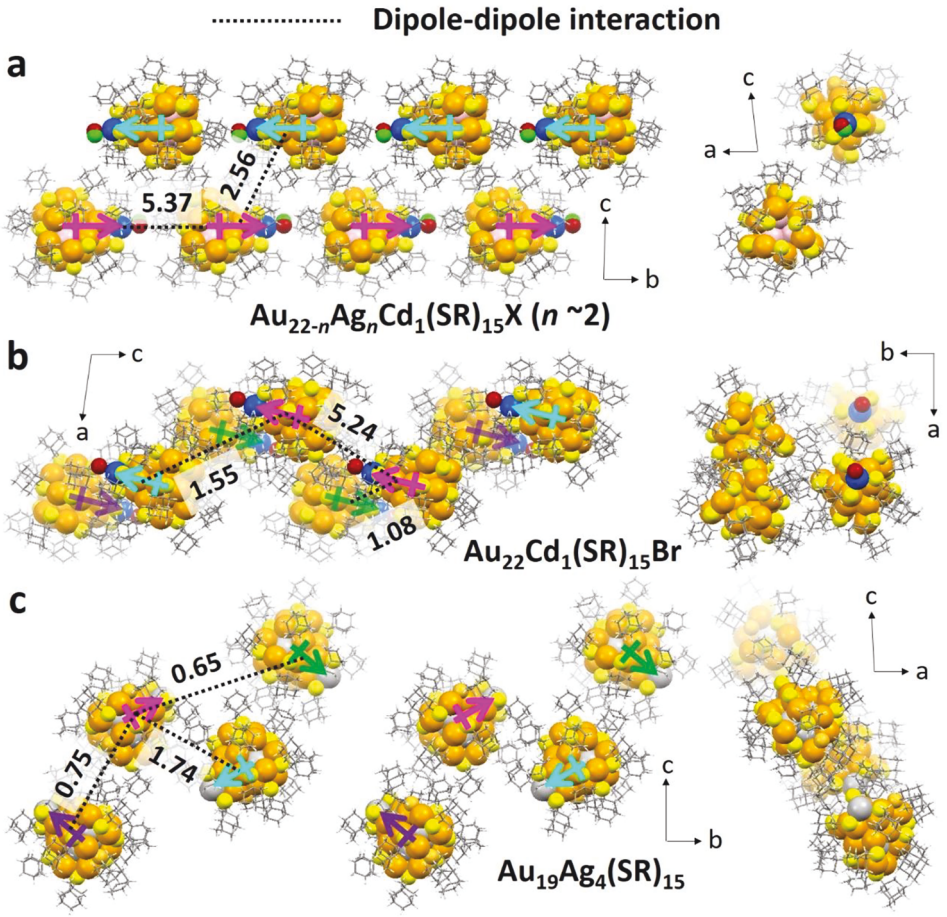

Figure 2. NC dipole alignment in the crystal states of (a) Au22-nAgnCd1(SR)15X (n = 1−4, X = Br/Cl), (b) Au22Cd1(SR)15Br, and (c) Au19Ag4(SR)15 (SR = SAdm). All NCs are marked with their dipole vectors, and the energy of attraction interactions between two NC dipoles are indicated in the unit of kJ/mol. Color labels: yellow = Au, light gray = Ag, pink = Au/Ag, blue = Cd, maroon = Br, green = Cl, light yellow = S, and gray = C.

shape (*i.e.*, symmetry) of the NCs, which is dictated by their protecting ligands, controls their permanent dipole moment. Thus, the occupancy of ligands at specific locations is also an important factor for the μ of nanoparticles. Herein, the atomically precise structures of a series of M_{23} NCs provide us with a great opportunity to fix the type and number of ligands as well as their overall arrangement (symmetry) on the NCs (Figure 1). Since heterometal-doping only affects atoms along the C_3 axis (Figure 1d) of the NCs, which is also the axis of their dipole moment vectors, we can directly probe the heterometal-doping effect on μ. Interestingly, we find an unexpected result that μ for $Au_{19}Ag_3Cd_1(SAdm)_{15}Br$, $Au_{22}Cd_1(SAdm)_{15}Br$, and $Au_{19}Ag_4(SAdm)_{15}$ is significantly larger, being 18.18 D, 17.07 D, and 10.72 D, respectively (Figure 1 and Table S3). Especially, the involvement of Br, which is added through Cd-doping as a consequence of the divalent nature of Cd, is believed to be responsible for the much higher μ for the first two NCs. Dipole moment depends on the magnitudes and directions of the polar bonds inside a molecule or nanoparticle. Thus, the distribution of the heteroatoms along the main axis must be fulfilled, and $Au_{22-n}Ag_nCd_1(SAdm)_{15}Br$ (n = 3 and 0) indeed shows a quasi-C_3 axis along which Br, Cd, central Au, and M_3 (M = Au/Ag) are sequentially arranged from top to bottom (Figure 1d). Such alignment of heteroatoms with different electronegativities contributes to the high μ of these NCs. It is worth noting that, for both wurtzite CdSe and zinc-blende ZnSe nanocrystals, the large permanent dipole moment is linearly dependent on the radius of the semiconductor core.[11] Herein, $\mu \approx 18$ D for the two Br-containing NCs (core radius ~5 Å) fits the plot of dipole moment versus the size of CdSe and ZnSe QDs (Figure S5),[11] indicating high dipole moments of our M_{23} NCs.

One may argue that the heteroatom effect induces electron transfer and thus might increase the dipole moment; we note that previous work theoretically replaced one staple-gold atom in $Au_{30}(SAdm)_{18}$[23] with a Ag heteroatom to break its symmetry, but μ only increased from 0 to 0.85 D.[19] Furthermore, we calculated the dipole moment of the experimentally determined $Au_{16}Ag_1(SAdm)_{13}$[24] and found a normal value of μ = 2.81 D (Table S3). Therefore, to obtain deeper insight into the unusually high μ of the M_{23} NCs, we sought for natural bond orbital charge analysis.[25] As shown in Figure S6, significant electron transfer is observed in the M_{23} series. For all three NCs, the central Au in the icosahedral M_{13} kernel holds −0.33 to −0.38 e, whereas Ag in the $Ag_1(SAdm)_3$ motif of $Au_{19}Ag_4(SAdm)_{15}$ shows +0.54 e, and Cd in the $Cd_1(SAdm)_3Br$ motif is even more positive (+1.2 e). Correspondingly, very negative charge is found on Br (−0.7 e). Such a significant electron transfer is consistent with the electronegativity of these atoms. Not only can the negative and positive centers be clearly observed in the M_{23} series but the

https://dx.doi.org/10.1021/acsnano.0c01000
ACS Nano 2020, 14, 6599−6606

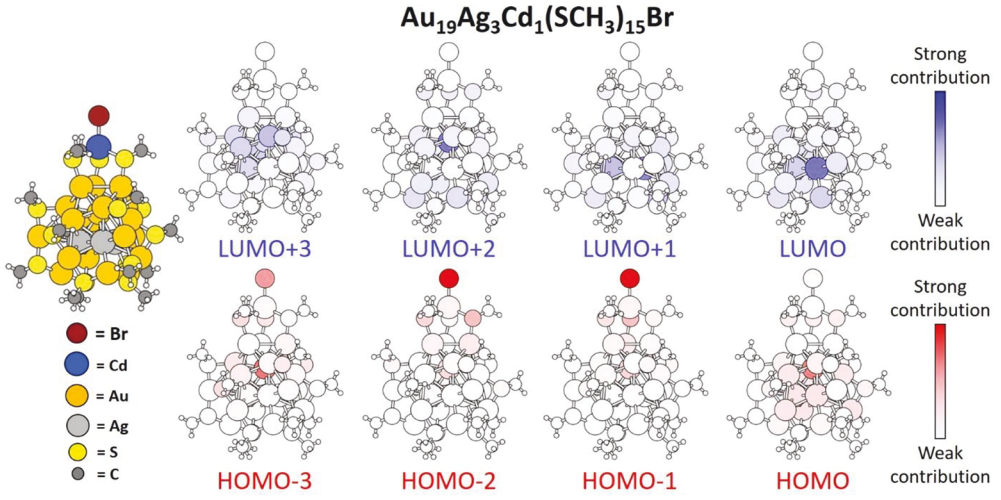

Figure 3. Mulliken contributions by different atoms to the KS frontier orbitals from HOMO−3 to LUMO+3 in $Au_{19}Ag_3Cd_1(SCH_3)_{15}Br$. Darker color (blue for LUMOs and red for HOMOs) corresponds to stronger contribution.

polar bonds are oriented in the same direction, hence giving rise to very high total dipole moments (see the guiding arrows in Figures S6). In other words, the charge separation is mainly along the quasi-C_3 axis of the M_{23} series in a parallel way, resulting in nearly zero μ_x and μ_y, and very large μ_z (Table S3). As a comparison, we also calculated the atomic charges of $[Au_{25}(SC_2H_4Ph)_{18}]^{0}$[26] (Figure S7). The $[Au_{25}(SC_2H_4Ph)_{18}]^0$ NC was selected due to its high stability and similar structural characteristics to the M_{23} series (similar size and 13-atom icosahedral kernel). Electron transfer is also found in $[Au_{25}(SC_2H_4Ph)_{18}]^0$ (Figure S7); however, the Au atoms on the shell are equally positive due to the centrosymmetric geometry, and the vectors are canceled out to give $\mu \approx 0$ for $[Au_{25}(SC_2H_4Ph)_{18}]^0$. Thus, electron transfer induced by heteroatom is not the main source of the high dipole moment observed in the current work. Instead, it is the special arrangement of the heteroatoms (along the C_3 axis) due to the symmetry of the M_{23} NCs. Furthermore, we note that the ligand occupancy of S-Adm around the C_3 axis does not change in the M_{23} series, enabling the NCs to maintain a similar overall structure. This result is important, as preserving the structure of NCs after undergoing ligand exchange as well as metal exchange is a key challenge to maintain the specific NC properties.

High μ of the M_{23} NCs leads to interesting alignment of NCs in the crystals (Figure 2). The trimetallic $Au_{22-n}Ag_nCd_1(SAdm)_{15}X$ (n = 1−4, X = Br/Cl) NCs are crystallized in P-1 space group (Figure 2a), and μ = 18.18 D of $Au_{19}Ag_3Cd_1(SAdm)_{15}Br$ is used to estimate the attraction energies (E) between the dipoles (see SI). It is observed that the NCs are aligned into "head-to-tail" cluster chains. Not only is the E within the chain (between two magenta NC dipoles) as high as 5.37 kJ/mol but that between two chains (between magenta and cyan NC dipoles) is 2.56 kJ/mol as well, indicating significant dipole−dipole interactions throughout the crystal (see dipole−dipole interaction energy calculation details in the SI). In previous work of quantum dot-to-nanowire growth, dipole attractions higher than the thermal energy RT (~2.5 kJ/mol) were reported to cause the oriented attachment, forming 1D nanostructures.[27] In the current work, dipolar attractions can also be the decisive force in directing the alignment of NCs.

The $Au_{22}Cd_1(SAdm)_{15}Br$ NCs (μ = 17.08 D) are crystallized in $P2_1/n$ space group (Figure 2b). The dipole−dipole attraction energy between two magenta NC dipoles is also high (5.24 kJ/mol), but the attractions between other NC dipoles are much lower (1.55 and 1.08 kJ/mol) than RT. Compared to the above trimetallic case, strong dipole−dipole interactions are found between some NCs in the crystal, but not in all dimensions. Thus, although the NC dipoles are aligned along the same direction, they are not in a line.

By comparison, for $Au_{19}Ag_4(SAdm)_{15}$ NCs (μ = 10.72 D), the interaction energies are calculated to be 1.74, 0.75, and 0.65 kJ/mol for various pairs (Figure 2c), much less than the regular value (~1.5 kJ/mol) for dipole−dipole interaction for molecules.[12] As a result, these NCs are not 1D aligned in the crystal.

Taken together, the alignment of M_{23} NCs in the crystal state can be controlled by their dipole moments, which can be tuned by heteroatom doping along the main axis. As a reference, assuming the NCs are lined up with a typical distance of 2 nm, the intercluster attraction energy is no more than 0.38 kJ/mol for NCs of μ = 5 D, much less than the regular molecular dipole−dipole interactions (~1.5 kJ/mol).[12] Thus, we do not expect strong interactions to occur in most Au-SR NCs. It should be noted that some other factors are also responsible for the NCs alignment in the crystal state, for example, symmetry, counterions,[28] *etc.*, but in our M_{23} series, the dipole−dipole interaction is the major reason.

As introducing Cd−Br bond into the metal-SR NCs is critical for high μ, we further explore the influence of Br atom on the frontier orbitals by TDDFT calculations. The optical absorption spectra of $Au_{19}Ag_3Cd_1(SR)_{15}Br$, $Au_{22}Cd_1(SR)_{15}Br$, and $Au_{19}Ag_4(SR)_{15}$ are simulated based on DFT-optimized structures from the original crystal structures. Figure S8 shows computed absorption spectra, the corresponding KS orbitals, and the origin of the HOMO−LUMO transitions for each NC. It is interesting to see that the element-type contributions to KS orbitals (*i.e.*, contributions from Au, Ag, S, *etc.*) near the HOMO and LUMO of the trimetallic $Au_{19}Ag_3Cd_1(SCH_3)_{15}Br$ (Figure S8b) share similarities with both the bimetallic $Au_{22}Cd_1(SCH_3)_{15}Br$ (Figure S8e) and $Au_{19}Ag_4(SCH_3)_{15}$ (Figure S8h). For example, the HOMO and LUMO of the trimetallic NC and $Au_{19}Ag_4(SCH_3)_{15}$ have nearly identical

https://dx.doi.org/10.1021/acsnano.0c01000
ACS Nano 2020, 14, 6599−6606

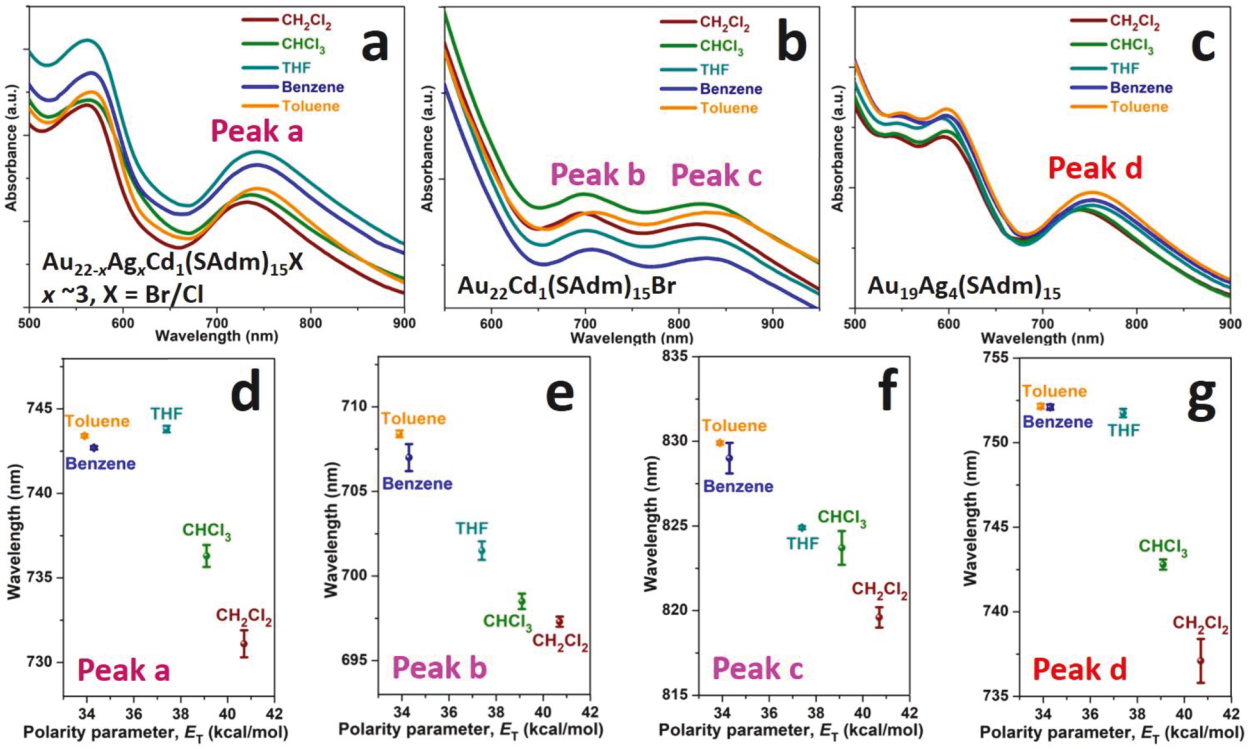

Figure 4. Solvent-dependent UV−vis spectra of (a) $Au_{22-n}Ag_nCd_1(SAdm)_{15}X$ (n = 2−8, X = Br/Cl), (b) $Au_{22}Cd_1(SAdm)_{15}Br$, (c) $Au_{19}Ag_4(SAdm)_{18}$, and (d−g) corresponding peak shift with respect to the polarity parameter (E_T) of different solvents taken from ref 32.

composition of element-type contributions, revealing the importance of the Ag_3 triangle in the kernel to the frontier orbital properties of the NCs. At the same time, the occupied orbitals just below the HOMO of $Au_{19}Ag_3Cd_1(SCH_3)_{15}Br$ NC resemble the HOMOs of the $Au_{22}Cd_1(SCH_3)_{15}Br$ NC, which can be attributed to the strong contributions from Br for both NCs.

The KS orbital diagram is commonly used to elucidate the transitions from occupied orbitals to unoccupied ones corresponding to the absorption peaks.[21,24,29] We herein provide a more explicit way to illustrate atomic contributions to the frontier orbitals by calculating Mulliken contributions (see Computational Details Section in SI). As shown in Figure 3, the atoms in $Au_{19}Ag_3Cd_1(SCH_3)_{15}Br$ that contribute more to the KS orbitals are marked in darker color (blue for unoccupied and red for occupied orbitals), while those contribute less are in lighter color (white indicates no contribution). These diagrams avoid summing up element-type contributions (*e.g.*, all Au atoms) and, instead, focus on the quota of each atom. Through this visualization scheme, we see that the LUMO/LUMO+1 are mainly localized on the bottom Ag_3 triangle in the kernel (Figure 3 top), and the HOMO is around the icosahedral central Au atom. As previously revealed in the KS orbital diagrams (Figure S8b), the HOMO-1/-2 states for $Au_{19}Ag_3Cd_1(SCH_3)_{15}Br$ (Figure 3 bottom) show a major contribution from the top Br, which is quite surprising for metal-SR NCs, as orbitals near the HOMO−LUMO gap are usually determined by the kernel atoms. The same is also found in $Au_{22}Cd_1(SCH_3)_{15}Br$ and $Au_{19}Ag_4(SCH_3)_{15}$ (see Figures S9 and S10 and KS Orbital Analysis in SI for more details). Importantly, the HOMOs and LUMOs of the M_{23} series are found to be located on different atoms, that is, a separation between the main atomic contributors of the HOMO/HOMO−1/-2 and LUMO/LUMO+1. This indicates that the transitions near the HOMO−LUMO gap occur across different atoms in the NCs (*i.e.*, charge transfer during excitation).

The large dipoles of the M_{23} NCs also led to strong interactions between NCs and solvent molecules in solution. Spectroscopic measurements based on solvent-sensitive standard compounds were previously used to determine the polarity of solvents, with the polarity parameter (E_T) defined as the molar transition energy (kcal/mol), which can be obtained from the experimental wavelength of the absorption maximum.[30] Kosower used 1-ethyl-4-methoxycarboyl-pyridinium as an indicator,[31] and a negative solvatochromism was observed, that is, the change of solvents from low to high polarity caused a hypsochromic shift (blue shift) of the absorption peak. Solvents of higher polarity will better stabilize the electronic ground state of the dye (an ion pair)[31] from becoming a radical pair in the first excited state.[32] Here, we have probed the solvent-dependent UV−vis spectra of the M_{23} NCs by using dichloromethane (CH_2Cl_2), chloroform ($CHCl_3$), tetrahydrofuran (THF), benzene, and toluene (Figure 4a−c). The absorption peaks of M_{23} NCs show distinct shifts (~25 meV) depending on the polarity of different solvents, suggesting strong interactions between solvents and NCs. Besides, the peak shifts are consistent with the polarity of the solvent measured by E_T values, indicating negative solvatochromism and charge-transfer transitions for the M_{23} NCs (Figure 4d−g). By contrast, $Au_{21}(SAdm)_{15}$,[21] $Au_{30}(S^tBu)_{18}$,[33] $[Au_{25}(SC_2H_4Ph)_{18}]^-$,[34] and $[Au_{25}(SC_2H_4Ph)_{18}]^0$[26] NCs show much smaller peak-shifts (<14 meV, Figure S11) due to their lower μ (0−4 D).

In addition to the ground-state charge transfer and large dipole moments, these M_{23} NCs also exhibit distinct excited-state charge transfer features, hence polar excited states as well. Femtosecond pump−probe spectroscopy was performed to

https://dx.doi.org/10.1021/acsnano.0c01000
ACS Nano 2020, 14, 6599−6606

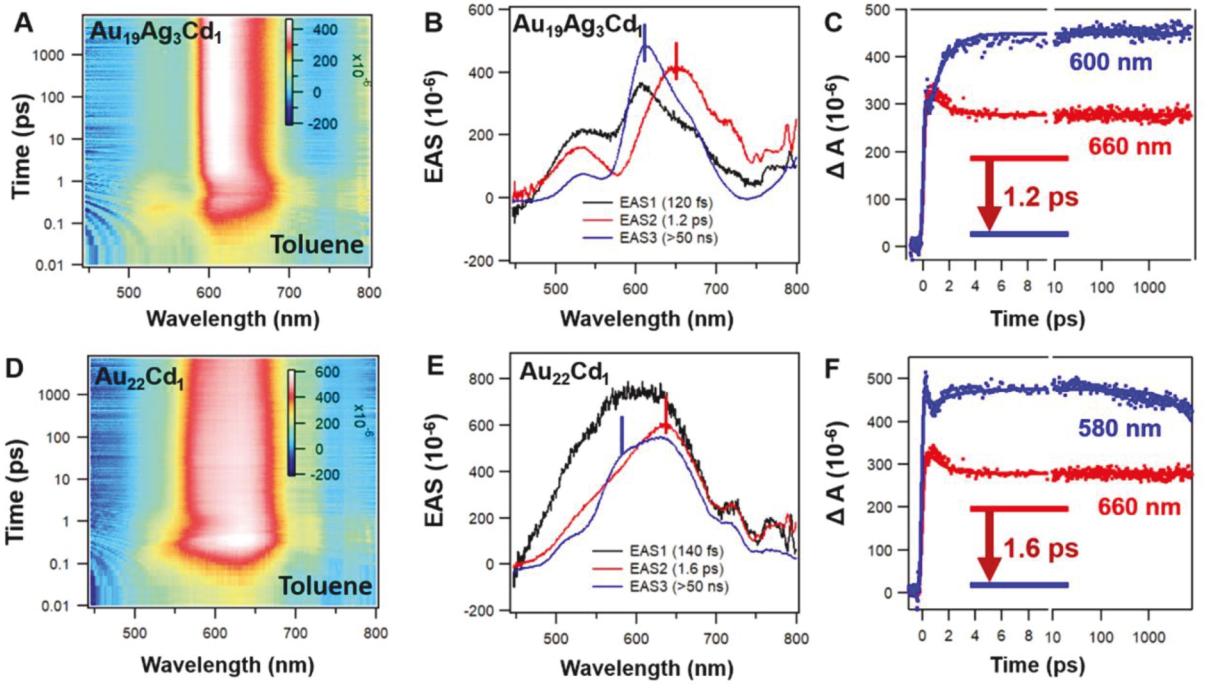

Figure 5. (A) TA data map of $Au_{19}Ag_3Cd_1$ with 400 nm excitation; (B) EAS of $Au_{19}Ag_3Cd_1$ obtained from global fitting; (C) kinetics and corresponding fits at selected wavelength from (A); (D) TA data map of $Au_{22}Cd_1$ with 400 nm excitation; (E) EAS of $Au_{22}Cd_1$ obtained from global fitting; (F) kinetics and corresponding fits at selected wavelength from panel D. Solvent: toluene.

probe the charge transfer behaviors of $Au_{19}Ag_3Cd_1$ and $Au_{22}Cd_1$ NCs in toluene. In the transient absorption spectra (TAS, ΔA) with 400 nm excitation (Figure 5A), broad excited state absorption (ESA) at 520 nm, 600 nm can be observed for $Au_{22-n}Ag_nCd_1(SAdm)X$ (n = 2−8, X = Br/Cl, abbrev. as $Au_{19}Ag_3Cd_1$), and there is no net ground state bleaching (GSB). The broad ESA decays within <1 ps, while between 0.8 and 3 ps, ESA around 660 nm experiences a prominent blueshift to 620 nm. A closer look at the TA spectra between 0.8 and 2.2 ps indicates an isosbestic point at 650 nm (Figure S12A), suggesting that the relaxation pathway follows a two-state model. Three decay components (120 fs, 1.2 ps and >50 ns) well fit the relaxation dynamics of $Au_{19}Ag_3Cd_1$ and the evolution associated spectra (EAS) obtained from global analysis clearly shows the evolution of the TAS (Figure 5B). Global fitting shows that both the decay of kinetics probed at 660 nm and the rise of kinetics probed at 600 nm occur in 1.2 ps (Figure 5C), which further validates the two-state model. In solution, upon photo excitation, an excited-state dipole will be generated in the solute (gold NC in our case). Subsequently, the solvent molecules will be reorganized around the surface of the solute (*i.e.*, solvation), which will decrease the energy of the excited state and give rise to the blueshift of ESA observed in Figure 5A. On the basis of previous studies, the solvation time varies between subpicosecond and a few ps depending on the polarity of solvent.[35] Because a ∼1 ps solvation time was observed in gold NCs dissolved in toluene,[36−38] the 1.2 ps process observed here can be assigned as the solvent stabilization of charge-transfer excited state. The $Au_{22}Cd_1(SAdm)_{15}Br$ (abbrev. as $Au_{22}Cd_1$) shows a broader ESA peak at 620 nm after excitation (Figure 5D). Between 0.8 and 2.8 ps, one can observe a similar blueshift in the ESA and an isosbestic point (Figure S12B). The EAS obtained from global fitting also gives three decay components, and both the rise probed at 580 nm and rapid decay probed at 660 nm occur in 1.6 ps (Figure 5E,F), similar to that observed in $Ag_{19}Ag_3Cd_1$, and the 1.6 ps component can also be assigned to the solvent stabilization of charge transfer states.

We further performed the TA experiment on both NCs dissolved in a different solvent ($CHCl_3$). A similar solvent stabilization process was observed (Figure S13). The solvent stabilization of excited states in both NCs confirmed that there are significant charge transfers in their excited states; thus, the excited states are also highly polar. Finally, nanosecond TA analyses (Figure S14) of $Au_{19}Ag_3Cd_1$ and $Au_{22}Cd_1$ NCs in toluene reveal that their excited state lifetimes are 340 and 258 ns, respectively. Taken together, the excited state characterization indicates highly polar excited states.

CONCLUSION

In summary, a series of atomically precise M_{23} NCs with high dipole moment is obtained, specifically, 18.18 and 17.08 D are found for $Au_{19}Ag_3Cd_1(SAdm)_{15}Br$ and $Au_{22}Cd_1(SAdm)_{15}Br$, respectively. A $Cd_1(SAdm)_3Br$ motif with Cd−Br ionic bond introduced on the surface of the NCs, and the heteroatom arrangement along the C_3 axis are responsible for achieving large dipole moments, fitting the experimental trend for II−VI QDs. Correspondingly, strong dipole−dipole interactions exceeding 5 kJ/mol for $Au_{22-n}Ag_nCd_1(SAdm)_{15}X$ can be observed in the crystal states, directing the NC dipoles in a "head-to-tail" alignment. Moreover, such interactions can be adjusted by doping-effected dipole moment. In solvent phases, the M_{23} series shows solvent-dependent absorption peak shifts of ∼25 meV, which trends well with the polarity of the solvents, demonstrating charge transfer absorption with negative solvatochromism. The ground state charge transfer, orbital localization, and absorption spectra analysis performed by DFT and TDDFT calculations reveal that the frontier orbitals, and thus the resulting excitations, involve completely different parts of the NCs. These properties offer fundamental

https://dx.doi.org/10.1021/acsnano.0c01000
ACS Nano 2020, 14, 6599−6606

understanding of the electronic properties of nanoclusters and may promote their future applications.

METHODS

Chemicals. Tetrachloroauric (III) acid ($HAuCl_4 \cdot 3H_2O$, 99.999% metal basis, Aldrich), silver nitrate ($AgNO_3$, > 99.0%, Aldrich), cadmium dichloride ($CdCl_2$, 99.99%, Aldrich), tetraoctylammonium bromide (TOABr, > 98%, Alfa Aesar), sodium borohydride ($NaBH_4$, 99.99% metal basis, Aldrich), 1-adamantanethiol (HSAdm, $HSC_{10}H_{15}$, 95%, Aldrich), 2-methyl-2-propanethiol (HS^tBu, 99%, Aldrich), 2-phenylethanethiol (HSC_2H_4Ph, 99%, Aldrich), tetrahydrofuran (THF, HPLC grade), ethanol (HPLC grade), methanol (HPLC grade), dichloromethane (CH_2Cl_2, HPLC grade), benzene (HPLC grade), toluene (HPLC grade), chloroform ($CHCl_3$, HPLC grade), and acetone (HPLC grade) were used as received.

Synthesis. To prepare $Au_{22-n}Ag_nCd_1(SAdm)_{15}(Br/Cl)$ (n = 1−4), 88.50 mg of $HAuCl_4 \cdot 3H_2O$, 1.14 mg of $AgNO_3$ (dissolved in 0.5 mL nanopure water first), 4.12 mg of $CdCl_2$ (dissolved in 0.5 mL nanopure water first) with Au/Ag/Cd molar ratio = 10:0.3:1, 150 mg of TOABr, and 120 mg of HS-Adm were mixed in THF and vigorously stirred for 30 min. Then a freshly prepared aqueous solution of $NaBH_4$ (144 mg in 5 mL) was added. After 3 h, the crude product was washed by methanol thoroughly, extracted by acetone, and further dissolved in a mixture of toluene and ethanol overnight. After the solvent was evaporated, $Au_{22-n}Ag_nCd_1(SAdm)_{15}(Br/Cl)$ nanoclusters were extracted by CH_2Cl_2. Plate-shaped crystals were obtained via solvent evaporation of methanol into a CH_2Cl_2 solution of the nanoclusters within 2 days.

To prepare $Au_{22-n}Ag_nCd_1(SAdm)_{15}(BrCl)$ (n = 2−8), only the Au/Ag/Cd molar ratio was changed to 10:0.5:1, and others remained the same, that is, 86.96 mg of $HAuCl_4 \cdot 3H_2O$, 1.87 mg of $AgNO_3$, and 4.05 mg of $CdCl_2$ were mixed. This experiment shows that the amount of Ag in $Au_{22-n}Ag_nCd_1(SAdm)_{15}(Br/Cl)$ can be readily controlled.

To prepare $Au_{22}Cd_1(SAdm)_{15}Br$, 92.31 mg of $HAuCl_4 \cdot 3H_2O$, 3.58 mg of $CdCl_2$ (dissolved in 1 mL of nanopure water first) with Au/Cd molar ratio = 12:1, 150 mg of TOABr, and 120 mg of HS-Adm were mixed in THF and vigorously stirred for 30 min. Then a freshly prepared aqueous solution of $NaBH_4$ (144 mg in 5 mL) was added. After 3 h, the crude product was washed by methanol thoroughly, extracted by acetone, and further dissolved in a mixture of toluene and ethanol for overnight. After evaporating the solvent, $Au_{22}Cd_1(SAdm)_{15}Br$ nanoclusters were extracted by CH_2Cl_2. Rod-shaped crystals were obtained via solvent evaporation of ethanol into a CH_2Cl_2 solution of the nanoclusters within 2 days.

ASSOCIATED CONTENT

Supporting Information

The Supporting Information is available free of charge at https://pubs.acs.org/doi/10.1021/acsnano.0c01000.

Details of characterizations, including UV−vis, ESI MS spectra, X-ray crystallography, TA analysis, dipole−dipole interaction, computational details, and KS orbital analysis; supporting Figures S1−S14 and Tables S1−S6 (PDF)

checkCIF/PLATON report of $Au_{22}Cd_1(SAdm)_{15}Br$ (PDF)

checkCIF/PLATON report of $Au_{22-n}Ag_nCd_1(SAdm)_{15}X$ (PDF)

AUTHOR INFORMATION

Corresponding Authors

Rongchao Jin − *Department of Chemistry, Carnegie Mellon University, Pittsburgh, Pennsylvania 15213, United States;* orcid.org/0000-0002-2525-8345; Email: rongchao@andrew.cmu.edu

Giannis Mpourmpakis − *Department of Chemical Engineering, University of Pittsburgh, Pittsburgh, Pennsylvania 15261, United States;* orcid.org/0000-0002-3063-0607; Email: gmpourmp@pitt.edu

Yongbo Song − *Department of Chemistry and Centre for Atomic Engineering of Advanced Materials, Anhui Province Key Laboratory of Chemistry for Inorganic/Organic Hybrid Functionalized Materials, Anhui University, Hefei, Anhui 230601, People's Republic of China*; Email: ybsong860@ahu.edu.cn

Authors

Yingwei Li − *Department of Chemistry, Carnegie Mellon University, Pittsburgh, Pennsylvania 15213, United States*

Michael J. Cowan − *Department of Chemical Engineering, University of Pittsburgh, Pittsburgh, Pennsylvania 15261, United States;* orcid.org/0000-0001-8706-782X

Meng Zhou − *Department of Physics, University of Miami, Coral Gables, Florida 33146, United States;* orcid.org/0000-0001-5187-9084

Michael G. Taylor − *Department of Chemical Engineering, University of Pittsburgh, Pittsburgh, Pennsylvania 15261, United States*

He Wang − *Department of Physics, University of Miami, Coral Gables, Florida 33146, United States;* orcid.org/0000-0003-1365-0304

Complete contact information is available at: https://pubs.acs.org/10.1021/acsnano.0c01000

Author Contributions

[¶]These authors contributed equally.

Notes

The authors declare no competing financial interest.

ACKNOWLEDGMENTS

R.J. and G.M. acknowledge the financial support from the National Science Foundation (NSF DMR-1808675 and CBET-CAREER program under Grant No. 1652694). Z.M. and H.W. acknowledge the financial support by the Air Force Office of Scientific Research (AFOSR) Award No. FA9550-17-1-0099. Computational support was provided by the Center for Research Computing (CRC) at the University of Pittsburgh as well as the Extreme Science and Engineering Discovery Environment (XSEDE), which is supported by the NSF (ACI-1548562).

REFERENCES

(1) Dresselhaus, M. S.; Chen, G.; Tang, M. Y.; Yang, R.; Lee, H.; Wang, D.; Ren, Z.; Fleurial, J.-P.; Gogna, P. New Directions for Low-Dimensional Thermoelectric Materials. *Adv. Mater.* **2007**, *19*, 1043−1053.

(2) Zabet-Khosousi, A.; Dhirani, A.-A. Charge Transport in Nanoparticle Assemblies. *Chem. Rev.* **2008**, *108*, 4072−4124.

(3) Redl, F. X.; Cho, K.-S.; Murray, C. B.; O'Brien, S. Three-Dimensional Binary Superlattices of Magnetic Nanocrystals and Semiconductor Quantum Dots. *Nature* **2003**, *423*, 968−971.

(4) Gao, J.; Zhang, B.; Zhang, X.; Xu, B. Magnetic-Dipolar-Interaction-Induced Self-Assembly Affords Wires of Hollow Nanocrystals of Cobalt Selenide. *Angew. Chem., Int. Ed.* **2006**, *45*, 1220−1223.

(5) Lan, X.; Wang, Q. Self-Assembly of Chiral Plasmonic Nanostructures. *Adv. Mater.* **2016**, *28*, 10499−10507.

(6) Nie, Z.; Petukhova, A.; Kumacheva, E. Properties and Emerging Applications of Self-Assembled Structures Made from Inorganic Nanoparticles. *Nat. Nanotechnol.* **2010**, *5*, 15−25.
(7) Zornberg, L. Z.; Gabrys, P. A.; Macfarlane, R. J. Optical Processing of DNA-Programmed Nanoparticle Superlattices. *Nano Lett.* **2019**, *19*, 8074−8081.
(8) Xia, Y.; Xiong, Y.; Lim, B.; Skrabalak, S. E. Shape-Controlled Synthesis of Metal Nanocrystals: Simple Chemistry Meets Complex Physics? *Angew. Chem., Int. Ed.* **2009**, *48*, 60−103.
(9) Jin, R.; Cao, Y.; Hao, E.; Metraux, G. S.; Schatz, G. C.; Mirkin, C. A. Controlling Anisotropic Nanoparticle Growth through Plasmon Excitation. *Nature* **2003**, *425*, 487−490.
(10) Blanton, S. A.; Leheny, R. L.; Hines, M. A.; Guyot-Sionnest, P. Dielectric Dispersion Measurements of CdSe Nanocrystal Colloids Observation of a Permanent Dipole Moment. *Phys. Rev. Lett.* **1997**, *79*, 865−868.
(11) Shim, M.; Guyot-Sionnest, P. Permanent Dipole Moment and Charges in Colloidal Semiconductor Quantum Dots. *J. Chem. Phys.* **1999**, *111*, 6955−6964.
(12) Tang, Z.; Kotov, N. A.; Giersig, M. Spontaneous Organization of Single CdTe Nanoparticles into Luminescent Nanowires. *Science* **2002**, *297*, 237−240.
(13) Cho, K.-S.; Talapin, D. V.; Gaschler, W.; Murray, C. B. Designing PbSe Nanowires and Nanorings through Oriented Attachement of Nanoparticles. *J. Am. Chem. Soc.* **2005**, *127*, 7140−7147.
(14) Kagan, C. R.; Murray, C. B.; Nirmal, M.; Bawendi, M. G. Electronic Energy Transfer in CdSe Quantum Dot Solids. *Phys. Rev. Lett.* **1996**, *76*, 1517−1520.
(15) Shevchenko, E. V.; Ringler, M.; Schwemer, A.; Talapin, D. V.; Klar, T. A.; Rogach, A. L.; Feldmann, J.; Alivisatos, A. P. Self-Assembled Binary Superlattices of CdSe and Au Nanocrystals and Their Fluorescence Properties. *J. Am. Chem. Soc.* **2008**, *130*, 3274−3275.
(16) Jin, R.; Zeng, C.; Zhou, M.; Chen, Y. Atomically Precise Colloidal Metal Nanoclusters and Nanoparticles: Fundamentals and Opportunities. *Chem. Rev.* **2016**, *116*, 10346−10413.
(17) Chakraborty, P.; Nag, A.; Chakraborty, A.; Pradeep, T. Approaching Materials with Atomic Precision Using Supramolecular Cluster Assemblies. *Acc. Chem. Res.* **2019**, *52*, 2−11.
(18) Chakraborty, A.; Fernandez, A. C.; Som, A.; Mondal, B.; Natarajan, G.; Paramasivam, G.; Lahtinen, T.; Häkkinen, H.; Nonappa; Pradeep, T. Atomically Precise Nanocluster Assemblies Encapsulating Plasmonic Gold Nanorods. *Angew. Chem.* **2018**, *130*, 6632−6636.
(19) Cowan, M. J.; Higaki, T.; Jin, R.; Mpourmpakis, G. Understanding the Solubility Behavior of Atomically Precise Gold Nanoclusters. *J. Phys. Chem. C* **2019**, *123*, 20006−20012.
(20) Li, Y.; Luo, T.-Y.; Zhou, M.; Song, Y.; Rosi, N. L.; Jin, R. A Correlated Series of Au/Ag Nanoclusters Revealing the Evolutionary Patterns of Asymmetric Ag Doping. *J. Am. Chem. Soc.* **2018**, *140*, 14235−14243.
(21) Chen, S.; Xiong, L.; Wang, S.; Ma, Z.; Jin, S.; Sheng, H.; Pei, Y.; Zhu, M. Total Structure Determination of $Au_{21}(S\text{-}Adm)_{15}$ and Geometrical/Electronic Structure Evolution of Thiolate Gold Nanoclusters. *J. Am. Chem. Soc.* **2016**, *138*, 10754−10757.
(22) Zeng, C.; Chen, Y.; Kirschbaum, K.; Appavoo, K.; Sfeir, M. Y.; Jin, R. Structural Patterns at All Scales in a Nonmetallic Chiral $Au_{133}(SR)_{52}$ Nanoparticle. *Sci. Adv.* **2015**, *1*, No. e1500045.
(23) Higaki, T.; Liu, C.; Zeng, C.; Jin, R.; Chen, Y.; Rosi, N. L.; Jin, R. Controlling the Atomic Structure of Au_{30} Nanoclusters by a Ligand-Based Strategy. *Angew. Chem., Int. Ed.* **2016**, *55*, 6694−6697.
(24) Kang, X.; Xiong, L.; Wang, S.; Pei, Y.; Zhu, M. Combining the Single-Atom Engineering and Ligand-Exchange Strategies: Obtaining the Single-Heteroatom-Doped $Au_{16}Ag_1(S\text{-}Adm)_{13}$ Nanocluster with Atomically Precise Structure. *Inorg. Chem.* **2018**, *57*, 335−342.
(25) Taylor, M. G.; Mpourmpakis, G. Thermodynamic Stability of Ligand-Protected Metal Nanoclusters. *Nat. Commun.* **2017**, *8*, 15988.
(26) Zhu, M.; Eckenhoff, W. T.; Pintauer, T.; Jin, R. Conversion of Anionic $[Au_{25}(SCH_2CH_2Ph)_{18}]^-$ Cluster to Charge Neutral Cluster *via* Air Oxidation. *J. Phys. Chem. C* **2008**, *112*, 14221−14224.
(27) Yu, J. H.; Joo, J.; Park, H. M.; Baik, S.-I.; Kim, Y. W.; Kim, S. C.; Hyeon, T. Synthesis of Quantum-Sized Cubic ZnS Nanorods by the Oriented Attachment Mechanism. *J. Am. Chem. Soc.* **2005**, *127*, 5662−5670.
(28) Li, Q.; Russell, J. C.; Luo, T.-Y.; Roy, X.; Rosi, N. L.; Zhu, Y.; Jin, R. Modulating the Hierarchical Fibrous Assembly of Au Nanoparticles with Atomic Precision. *Nat. Commun.* **2018**, *9*, 3871.
(29) Yang, S.; Chai, J.; Song, Y.; Fan, J.; Chen, T.; Wang, S.; Yu, H.; Li, X.; Zhu, M. *In Situ* Two-Phase Ligand Exchange: A New Method for the Synthesis of Alloy Nanoclusters with Precise Atomic Structures. *J. Am. Chem. Soc.* **2017**, *139*, 5668−5671.
(30) Katritzky, A. R.; Fara, D. C.; Yang, H.; Tämm, K.; Tamm, T.; Karelson, M. Quantitative Measures of Solvent Polarity. *Chem. Rev.* **2004**, *104*, 175−198.
(31) Kosower, E. M. The Effect of Solvent on Spectra. I. A New Empirical Measure of Solvent Polarity: Z-Values. *J. Am. Chem. Soc.* **1958**, *80*, 3253−3260.
(32) Reichardt, C.; Welton, T. *Solvents and Solvent Effects in Organic Chemistry*, 4th ed.; John Wiley & Sons: Weinheim, 2011; pp 448−481.
(33) Crasto, D.; Malola, S.; Brosofsky, G.; Dass, A.; Häkkinen, H. Single Crystal XRD Structure and Theoretical Analysis of the Chiral $Au_{30}S(S\text{-}t\text{-}Bu)_{18}$ Cluster. *J. Am. Chem. Soc.* **2014**, *136*, 5000−5005.
(34) Zhu, M.; Aikens, C. M.; Hollander, F. J.; Schatz, G. C.; Jin, R. Correlating the Crystal Structure of a Thiol-Protected Au_{25} Cluster and Optical Properties. *J. Am. Chem. Soc.* **2008**, *130*, 5883−5885.
(35) Ramakrishna, G.; Bhaskar, A.; Goodson, T. Ultrafast Excited State Relaxation Dynamics of Branched Donor-π-Acceptor Chromophore: Evidence of a Charge-Delocalized State. *J. Phys. Chem. B* **2006**, *110*, 20872−20878.
(36) Zhou, M.; Vdović, S.; Long, S.; Zhu, M.; Yan, L.; Wang, Y.; Niu, Y.; Wang, X.; Guo, Q.; Jin, R.; Xia, A. Intramolecular Charge Transfer and Solvation Dynamics of Thiolate Protected $Au_{20}(SR)_{16}$ Clusters Studied by Ultrafast Measurement. *J. Phys. Chem. A* **2013**, *117*, 10294−10303.
(37) Zhou, M.; Lei, Z.; Guo, Q.; Wang, Q.-M.; Xia, A. Solvent Dependent Excited State Behaviors of Luminescent Gold(I)-Silver(I) Cluster with Hypercoordinated Carbon. *J. Phys. Chem. C* **2015**, *119*, 14980−14988.
(38) Zhou, M.; Yao, C.; Sfeir, M. Y.; Higaki, T.; Wu, Z.; Jin, R. Excited-State Behaviors of $M_1Au_{24}(SR)_{18}$ Nanoclusters: The Number of Valence Electrons Matters. *J. Phys. Chem. C* **2018**, *122*, 13435−13442.

https://dx.doi.org/10.1021/acsnano.0c01000
ACS Nano 2020, 14, 6599−6606